

3-D lithospheric structure beneath southern Tibet from Rayleigh-wave tomography with a 2-D seismic array

Mingming Jiang,^{1,2} Shiyong Zhou,¹ Eric Sandvol,³ Xiaofei Chen,⁴ Xiaofeng Liang,^{1,3} Y. John Chen¹ and Wenyuan Fan¹

¹*Institute of Theoretical and Applied Geophysics, Peking University, Beijing 100871 China. E-mail: zsy@pku.edu.cn*

²*Key Laboratory of the Earth's Deep Interior, Institute of Geology and Geophysics, Chinese Academy of Science, Beijing 100029 China*

³*Department of Geological Sciences, University of Missouri-Columbia, Columbia, MO 65211, USA*

⁴*School of Earth and Space Sciences, University of Science and Technology of China, Hefei 230026 China*

Accepted 2011 January 31. Received 2011 January 28; in original form 2010 July 6

SUMMARY

A 3-D shear wave velocity model has been established for the lithosphere of southern Tibet through Rayleigh-wave tomography. The teleseismic data are acquired from a 2-D seismic array selected out of the second phase of the Hi-CLIMB project. We first inverted for a 2-D phase velocity model using two-plane-wave tomography approach, and then inverted for the 3-D shear wave velocity model with the 2-D phase velocity model and the map of crustal thickness derived from receiver functions. The results reveal a pervasive low velocity anomaly in the middle crust of the Lhasa block. We interpret this low velocity anomaly as the presence of wholesale mid-crustal channel flow. Prominent low velocity anomalies from the lower crust to the mantle lithosphere are observed along the north–south trending rifts: the Tangra Yum Co rift and the Pumqu Xianza rift. We propose a possible scenario for the formation of these rifts: the entire lithosphere is involved in the early-stage rifting, while the late-stage rifting is restricted in the upper crust. In the non-rift regions, a slab-like high velocity anomaly is traced beneath both the Himalayas and Lhasa block. Combining all the observations, we suggest that the central part of southern Tibet is currently underlain by the broken Indian lower crust and mantle lithosphere.

Key words: Surface waves and free oscillations; Seismic tomography; Continental margins: convergent; Dynamics: seismotectonics; Crustal structure.

1 INTRODUCTION

The typical example of active continental collision is the Himalayas and Tibetan plateau caused by the collision between the Indian and Asian Plates starting around 55 Ma (Patriat & Achache 1984; Besse *et al.* 1984). As a result of this collision, the Himalayas are the highest range on the earth and the Tibetan plateau has an average altitude of ~5000 m and an abnormally thickened crust, approximately twice the average thickness of continental crust. Despite the great efforts made to investigate the Himalayas and Tibetan plateau, the tectonic processes that form the plateau are still under debate. Several candidate models were presented for explaining the broad and uniform crustal thickening of the Tibetan plateau: (1) subhorizontal underthrusting of the Indian lithosphere beneath the plateau (Argand 1924; Powell & Conaghan 1975; Ni & Barazangi 1984), (2) homogeneous thickening of the southern Asian lithosphere by distributed thrust faulting (Dewey & Burke 1973; Toksoz & Bird 1977), (3) lateral extrusion of thickened blocks along strike-slip faults (Molnar & Tapponnier 1975; Tapponnier & Molnar 1977) and (4) injection of the Indian crust into the Asian crust along

with underthrusting of the Indian continental lithosphere (Zhao & Morgan 1987). Although numerous models have been proposed, direct observational constraints on the lithospheric structure are still needed to evaluate these models and understand the formation of the high plateau.

As more and more investigations and experiments, such as PASSCAL 1991/1992 (Owens *et al.* 1993), INDEPTH (Zhao *et al.* 1993), INDEPTH II (Nelson *et al.* 1996), INDEPTH III (Zhao *et al.* 2001), HIMNT (Monsalve *et al.* 2006), Hi-CLIMB (Nabelek *et al.* 2009), INDEPTH IV (Zhao *et al.* 2007), have been conducted in and near the Tibetan plateau, a rough lithospheric structure of the plateau has been retrieved. The crustal structure is well constrained: The Main Himalayan thrust, along which the Indian lithosphere underthrusts beneath the Himalayas and Tibet plateau, is imaged to extend northward to at least the Indus Tsangpo suture (ITS, Zhao *et al.* 1993; Brown *et al.* 1996; Nelson *et al.* 1996; Wittlinger *et al.* 2004; Schulte-Pelkum *et al.* 2005). The presence of aqueous fluids and/or partial melts in the upper and/or middle crust of southern Tibet is certified by multidiscipline investigations (Brown *et al.* 1996; Makovsky *et al.* 1996; Nelson *et al.* 1996; Wei *et al.* 2001;

Xie *et al.* 2004; Unsworth *et al.* 2005). High temperature and partial melting from the lower crust to the uppermost mantle through central Tibet are implied (Rodgers & Schwartz 1998; Wei *et al.* 2001; Ross *et al.* 2004; Xie *et al.* 2004). North of the Jinsha River suture, there is partial melting in the crust and the crustal thickness is much thinner than in central Tibet (Wittlinger *et al.* 1996; Vergne *et al.* 2002). However, the structure of the mantle lithosphere is much less resolved. How far the Indian lithosphere advances northward is still controversial. Estimation of the collisional shortening tends to put the Indian lithosphere beneath the entire plateau (Wang *et al.* 2001; DeCelles *et al.* 2002; Johnson 2002). However, Tilmann *et al.* (2003) argued that the Indian Lithosphere reached the Bangong Nuijiang suture (BNS) and bent down subvertically into the deep mantle. Hoke *et al.* (2000) found the evidence that the Indian lithosphere started to subduct into the deep mantle near the ITS. Recently, Li *et al.* (2008) pointed that the horizontal distance, over which the Indian lithosphere slid northward, decreased from west to east along the Himalayan arc. The paradoxical conclusions on the mantle lithosphere are mainly due to the spatial limitation of the investigations and experiments and drawn using the data acquired from the north–south (N–S) trending linear arrays. However, the seismic tomography studies (Griot *et al.* 1998; Friederich 2003; Zhou & Murphy 2005; Li *et al.* 2008; Ren & Shen 2008; Hung *et al.* 2010; Liang *et al.* 2011) indicate that the heterogeneity in the Tibetan lithosphere is distributed in a 3-D fashion. Therefore, an elaborate 3-D lithospheric structure is necessary to reveal the tectonic processes of the Tibetan plateau.

The north–south (N–S) trending rifts are significant tectonic features in southern and central Tibet (Molnar & Tapponnier 1978; Tapponnier *et al.* 1981; Rothery & Drury 1984; Armijo *et al.*, 1986, 1989). They are commonly attributed to the east–west (E–W) extension of the plateau, perpendicular to India–Eurasia collision. There are two kinds of competitive models presented for the E–W extension. The first one relates the extension to gravitational collapse after an abrupt uplift of the plateau (England & Houseman 1989; Liu & Yang 2003). The second kind of models explains the extension by oblique convergence between Indian and Eurasian Plates (McCaffery & Nabelek 1998; Tapponnier *et al.* 2001). The formation of these rifts during the E–W extension is also controversial (e.g. Masek *et al.* 1994; Yin 2000). Recent body tomography studies in southern and southeastern Tibet indicate low velocity anomalies appear from the crust to upper mantle beneath the Tangra Yum Co rift (TYR, Liang *et al.* 2011), the Yadong-Gulu rift (YGR, Hung *et al.* 2010; Liang *et al.* 2011) and the Coma rift (Ren & Shen 2008).

Surface wave tomography is a powerful tool to detect the lithospheric structure precisely, especially for the mantle lithosphere. Because of both lack of 2-D seismic arrays with dense stations and surface wave tomography methods on regional arrays, high-resolution surface wave tomography studies are seldom conducted in the Tibetan plateau. Of the few studies, Yao *et al.* (2006, 2008) obtained a 3-D shear wave velocity model in southeastern Tibet from the combined analysis of ambient noise and teleseismic data. Nevertheless, there still are some surface wave dispersion studies on the Tibet plateau using very sparse seismic data. For example, Cotte *et al.* (1999) found the crustal structure contrast between north and south of the ITS in southern Tibet by dispersion and amplitude analysis of teleseismic Rayleigh waves using the INDEPTH II data; Rapine *et al.* (2003) measured the surface wave dispersions of five earthquakes recorded by the INDEPTH III array and revealed the very different crustal structures between southern and central Tibet. These pioneering studies provide valuable experiences for the future surface wave tomography studies on the Tibetan plateau.

In this paper, we have the opportunity to analyse the data acquired from a high station-density, well-distributed array in southern Tibet, which is a part of the Hi-CLIMB project (Himalayan–Tibetan Continental Lithosphere during Mountain Building, Nabelek *et al.* 2009). This array was deployed in a blank region, which was less studied in the past. In addition, with two-plane-wave tomography technique (Li *et al.* 2003; Forsyth & Li 2005), which models the incoming wavefield (fig. 4 of Forsyth & Li 2005) as the interference of two plane waves, we are able to obtain a 2-D precise phase velocity model. Then we invert for a 3-D shear wave velocity model with the determined phase velocities. Finally, we discuss the tectonic implications from our results.

2 DATA AND METHODOLOGY

We use the vertical component data from the second phase of the international collaborative Hi-CLIMB project. The second phase of the Hi-CLIMB project consists of two parts: the main N–S trending linear array and the complementary regional array, and records data continuously from 2004 July to 2005 August (Liang *et al.* 2008; Nabelek *et al.* 2009). We select a 2-D array out of the whole array (Fig. 1): 33 stations with three types of sensors (Guralp CMG-3ESP, Nanometrics Trillium40, Streckeisen STS-2) from the regional array and five stations with two types of sensors (Guralp CMG-3T, Streckeisen STS-2) from the southernmost part of the linear array. Our array spans ~500 km in E–W direction and ~300 km in N–S direction across the ITS. It situates in the blank region between the linear Hi-CLIMB array and the INDEPTH array and its southernmost part overlaps the HIMNT array. The distance between adjacent stations is 25–50 km.

2.1 Two-plane-wave Tomography

The seismograms of the earthquakes in a distance range of 33° – 120° with $M_S \geq 5.0$ are first cut from the raw data automatically. Because the background noise in Tibet is very low, we are able to obtain 81 events with high-quality seismograms. The backazimuthal distribution of these events is not very good (Fig. 2). Most of them locate on the boundary of the Pacific Plate east of our array. But still some events locate west of our array, which are important for solving for the lateral variations of phase velocities. The ray path coverage is excellent within the array and in the surrounding regions except for the west of the array (Fig. 3).

Fundamental mode Rayleigh waveforms are filtered and cut at 11 frequency bands, ranging from 7 to 40 mHz (25 to 143 s for period). We first normalize the instrument responses to the reference type (Streckeisen STS-2 sensor and REFTEK RT72A DAS), and then filter the seismograms with narrow bandpass filters for different frequency bands. The filter is a 10-mHz-wide, zero-phase-shift, four order, bandpass Butterworth filter centred at the frequency of interest. The Rayleigh waveforms are then cut by the time windows with cosine tapers on both ends from the filtered seismograms. Start time and length of the time windows are determined on epicentral distances and dispersion characters. The window length is equal for the same event at a frequency band. For each event at a frequency band, we plot all the Rayleigh waveforms together in order of epicentral distances. Waveforms with incoherent phases and amplitudes from station to station, as well as low SNR and very complicated waveform, can be easily identified and are removed from the data set. Furthermore, we check the misfits of the Rayleigh waveforms used in the inversion for 2-D isotropic phase velocities and remove the

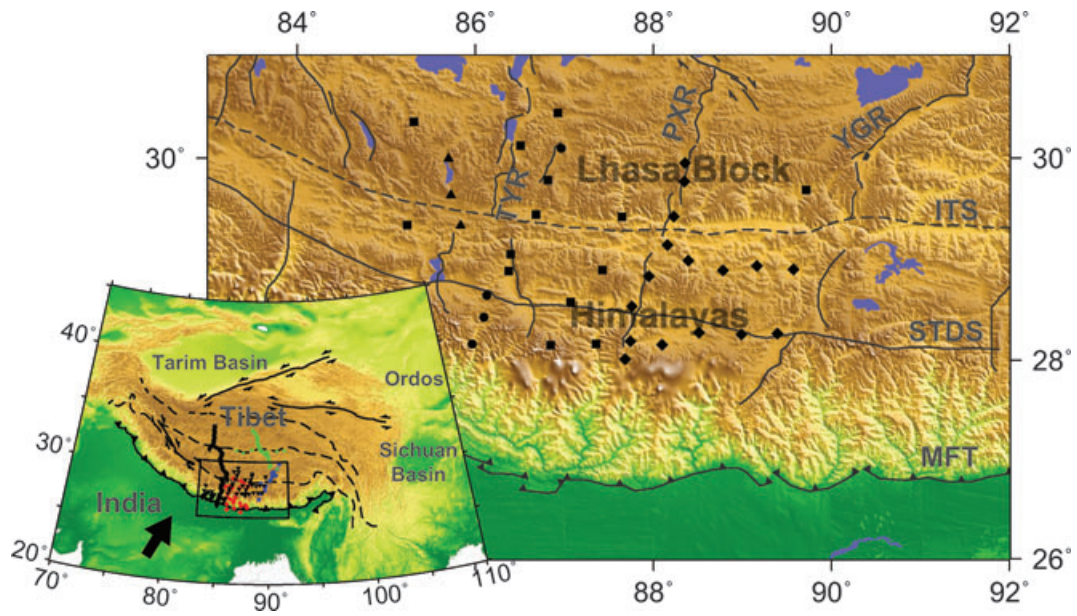


Figure 1. Topographic map of the study region in southern Tibet and broad-band seismic stations selected out of the Hi-CLIMB array. In the main figure, the stations are shown with different symbols representing different types of instruments: Black squares denote stations with the STS-2 sensors, black triangles denote stations with the CMG-3T sensors, black diamonds denote stations with the Trillium-40 sensors. The main tectonic boundaries and the N–S trending rifts are shown as: MFT, Main Frontal Thrust; STDS, Southern Tibet Detachment System; ITS, Indus Tsangpo Suture; TYR, Tangra Yum Co rift; PXY, Pumqu-Xianza rift; YGR, Yadong Gulu rift. In the inset map, the study region is outlined by the open box. The seismic arrays deployed by INDEPTH II, INDEPTH III, HIMNT, Hi-CLIMB are shown with black inverse triangles, blue squares, green triangles and red diamonds, respectively.



Figure 2. Azimuthal distribution of the teleseismic events used in this study. Epicentral distance from the centre of the seismic array is shown with concentric circles with degrees on the great circle.

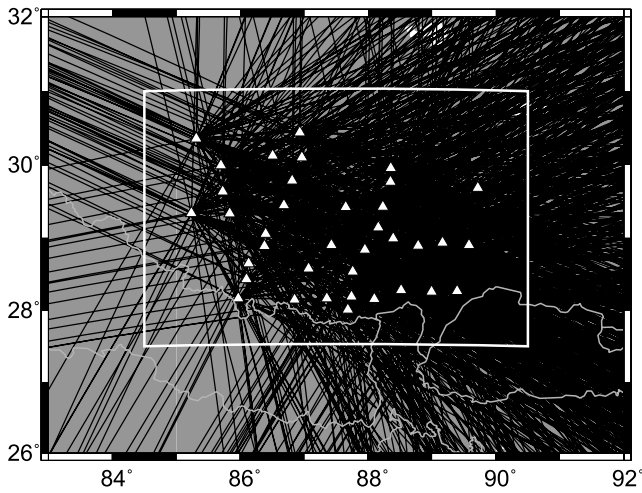


Figure 3. Great circle ray path coverage at the period of 50 s. The study region is marked with the open box. The ray path coverage is excellent within the study region except for the western edge.

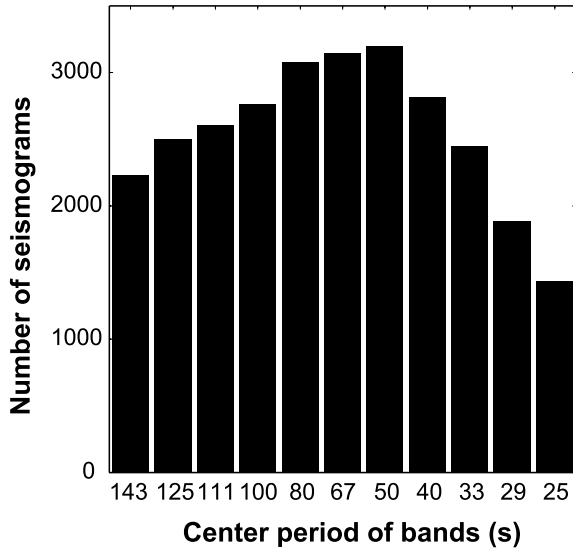


Figure 4. Numbers of the Rayleigh waveforms used at all periods of 25–143 s in the inversions for phase velocities.

waveforms with large misfits. If the good Rayleigh waveforms are fewer than 12, the event at the frequency band will be removed completely, that ensures sufficient information left to invert for phase velocities besides the wavefield parameters (Forsyth & Li 2005). Our final data set consists of ~30 000 Rayleigh waveforms (Fig. 4). The amplitudes and phases of Rayleigh waveforms are measured with a positive Fourier transform as two types of independent input data for inversions. The amplitudes are corrected for geometric spreading, anelastic attenuation using the formula

$$A_i = A_i^0 \exp(\gamma \Delta_i) [\sin(\Delta_i \pi / 180)]^{1/2} \quad (1)$$

where A_i^0 is the amplitude at the i th station before the correction, Δ_i is the epicentral distance to the i th station and γ is the anelastic attenuation coefficient which varies with frequency. The values of γ are determined on the studies of tectonically active regions (Mitchell 1995).

Considering the ray path coverage at each frequency band, we delimit the study region spanning from 84.5 to 90.5°E in longitude and from 27.5 to 31°N in latitude (Fig. 3). The study region is

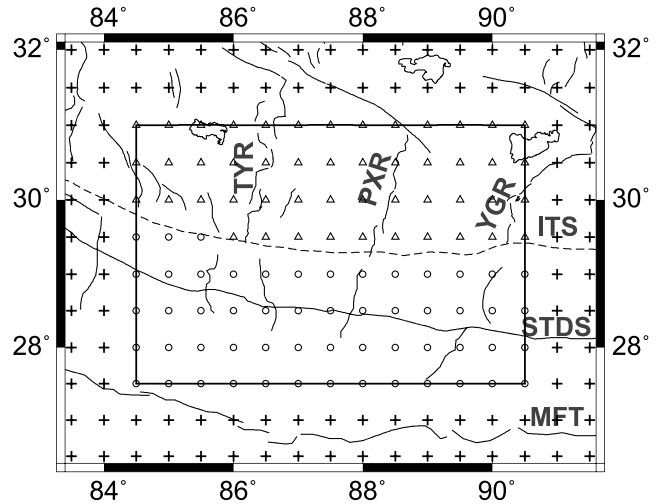


Figure 5. 2-D Grid of phase velocity model. The study region is marked with the open box. Within the study region, different symbols denote two different tectonic provinces: triangles for the Lhasa block, circles for the Himalayas. Two extra loops of grid nodes (crosses) outside the study region are used to ‘absorb’ some of the phase effects of complex incoming wavefields, which are not properly represented by the interference of two plane waves. The main tectonic boundaries and the N–S trending rifts are marked with the abbreviations as same as in Fig. 1.

parameterized with a 2-D grid (Fig. 5). The grid nodes are evenly distributed with a spacing of 0.5° in longitude and 0.5° in latitude. The nodes are divided into two groups for the Himalayas and the Lhasa block. Phase velocities are allowed to vary at each node in the 2-D inversions. Outside the study region, we add two extra loops of grid nodes with the same spacing and set their priori velocity errors as 10 times as those of the interior nodes in the inversions. This strategy can reduce the influence to the study region by the phase effects of very complex wavefields that cannot be well modelled by two plane waves (Li *et al.* 2003). The phase velocity at each node is defined by (Smith & Dahlen 1973)

$$c_i = B_{0,i} + B_{1,i} \cos 2\theta_i + B_{2,i} \sin 2\theta_i, \quad (2)$$

where i is the serial number of nodes, θ is the azimuth, B_0 is the isotropic phase velocity, B_1 and B_2 are the anisotropic terms. In the inversions for isotropic phase velocities, B_1 and B_2 are set to zero at each node. Before taken into the inversions, the grid velocity model is needed to reform to a spatial continuous function with a 2-D Gaussian function (Forsyth & Li 2005). The phase slowness function is defined by

$$S = \sum_{i=1}^N \frac{w_i}{c_i} / \sum_{i=1}^N w_i, \quad (3)$$

where N is the total number of grid nodes, c is the phase velocity at the i th node (eq. 2), w_i is the 2-D Gaussian function is defined by

$$w_i = \exp \left[-\frac{(x - x_i)^2 + (y - y_i)^2}{L_w^2} \right], \quad (4)$$

where (x_i, y_i) is the coordinate of the i th node, L_w is the scale length which trade-off model errors and model resolution in the inversions (Li *et al.* 2003). We have tried different L_w from 30 to 120 km and checked the trade-off between the model errors and misfits of data (Fig. 6). The model errors and misfit of data in Fig. 6 are the rms of rms errors and misfits of the inversions over all the frequency bands. We choose the scale length of 60 km in this study according to the trials.

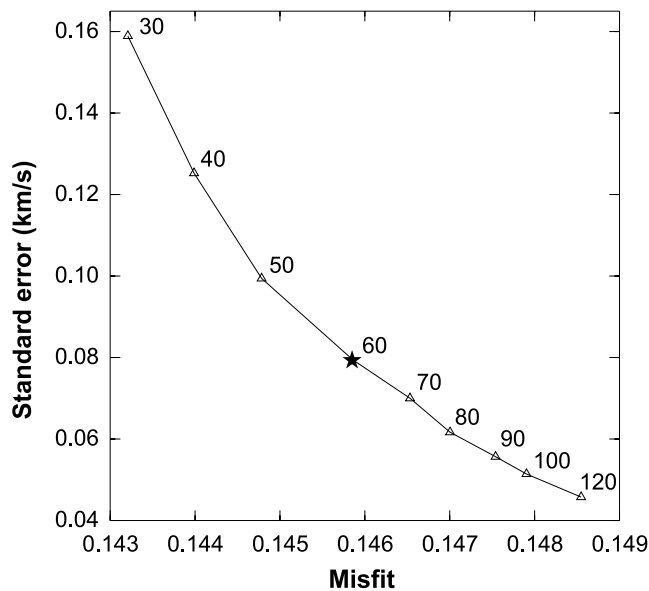


Figure 6. Trade-off curve between model standard errors and misfits of data in the inversions for 2-D isotropic phase velocity model. The trade-off is modified by the characteristic scale length L_W (km) in the 2-D Gaussian spatial weighting function (eq. 4). The model standard errors and the misfits of data are the rms of rms through all the frequency bands. The black star marks the selected value for the scale length L_W .

For each frequency band, the phase velocities are obtained by iteration. The incoming wavefield of each event is fitted by the interference of two plane waves with different amplitudes, phases and propagating directions. After carefully checking the waveforms mentioned above, the events, whose incoming wavefields are too complex to be fitted by two plane waves, are quite rare. Even if a few of such events are still in the final data set, their influence will be reduced by automatically assigning them small weighing factors in the inversions. According to Forsyth & Li (2005), there are two steps in one iteration. The six wavefield parameters of each event are inverted first by the simulated annealing method. Then a joint inversion for both phase velocities and wavefield parameters is conducted with the generalized non-linear least-squares algorithm (Tarantola & Valette 1982). After one iteration, the priori standard deviations of data in the next iteration are set to the posteriori standard deviations, and the weighting factors are set to the reciprocal of the standard deviations. So the influence of ‘bad’ events is reduced. The iteration repeats towards the final solution. In this study, the priori phase velocity errors are set to 0.2 km s^{-1} for all nodes inside the study region and 2.0 km s^{-1} for the two loops of surrounding nodes. The priori standard deviations of data are initially set to 0.1.

2.2 Shear velocity inversion

With the 2-D phase velocity structure as input data, we can establish the 3-D shear wave velocity structure. We invert for 1-D shear wave velocity model at each node in the 2-D phase velocity model and combine the 1-D shear wave velocity models to create a 3-D shear wave velocity model. The inversion procedure adopted in this study was first used by Weeraratne *et al.* (2003) and Li & Burge (2006). The derivatives of phase velocities with respect to densities and body wave velocities are calculated based on the method of Saito (1988). The invert method is still the generalized non-linear least-squares algorithm (Tarantola & Valette 1982). A layered model is introduced to represent the 1-D shear wave velocity structure. It

contains 16 layers from the Earth’s surface to the bottom of upper mantle (410 km) including three layers in the crust. Below 410 km, the Earth model maintains the AK135 model (Kennett *et al.* 1995). Layer thickness is $\sim 25 \text{ km}$ near the Earth’s surface and $\sim 50 \text{ km}$ near the bottom of upper mantle. The thickness of the two layers adjacent to the Moho can vary with the Moho depth. Phase velocities of Rayleigh waves are primarily sensitive to shear wave velocities, and insensitive to P -wave velocities deeper than $\sim 50 \text{ km}$. We keep the densities and V_p/V_s ratios unchanged in the inversions. We use a constant V_p/V_s ratio of 1.72 in the crust derived from the receiver function studies (Jin *et al.* 2006; Nabelek *et al.* 2009; Wittlinger *et al.* 2009). The V_p/V_s ratios in the mantle and the densities follow the AK135 model (Kennett *et al.* 1995). Therefore, the model parameters in the inversions are reduced to 17 (16 for shear wave velocities and 1 for Moho depth).

As an undetermined inversion problem, the inversions for shear wave velocities can yield a rational solution depending on the proper dumping and smoothing strategy as well as the initial model close to the real. We assign a priori model error of 0.1 km s^{-1} for dumping the shear wave velocities and a correlation coefficient of 0.4 between adjacent layers for smoothing the model. Particularly, no smoothness is assigned between the top four layers in the model. We have also tried different priori model errors from 0.05 km s^{-1} to 0.3 km s^{-1} and selected the proper value to make the resultant model more smooth and vary as much as possible from the initial model. Although the Moho depth is less constrained by Rayleigh-wave phase velocities, we can obtain precise initial Moho depth from receiver function studies. So we assign a small priori model error of 2 km for dumping the Moho depth.

3 RESULTS

3.1 Isotropic phase velocities

We have first inverted for the average phase velocity in the entire study region at each frequency band. The initial average phase velocities are from the dispersion curve of AK135 global model (Kennett *et al.* 1995). Both the initial AK135 phase velocities and the resultant average phase velocities in southern Tibet are shown in Fig. 7(a). The average phase velocities in southern Tibet are integrally lower than the global averages. Compared with the results in western China (Yao *et al.* 2005), the average phase velocities in southern Tibet at the periods shorter than $\sim 70 \text{ s}$ are prominently low, but at longer periods the difference of phase velocities is insignificant. Recalling that Rayleigh waves at the periods shorter than $\sim 70 \text{ s}$ mainly sample the crustal structure of Tibet, we suppose that the crustal structure of southern Tibet is a very special case in western China. For example, the average crustal thickness in western China is $\sim 50 \text{ km}$, while the crustal thickness in southern Tibet is more than 60 km . The abnormally thickened crust in southern Tibet may partly account for the low phase velocities at short periods. The model standard deviations originated from inversion algorithm are fairly small because of only one model parameter in the inversions (Fig. 7).

We have also inverted for the average phase velocities in the Himalayas and the Lhasa block (Fig. 7b). In the inversions, the nodes in the velocity model were divided into two groups (Fig. 5), and two-phase velocity parameters for two blocks are solved simultaneously. At all periods, the average phase velocities in the Himalayas are $\sim 0.05 \text{ km s}^{-1}$ higher than those in the Lhasa block, that reflects different lithospheric structures of two blocks in consistent with the

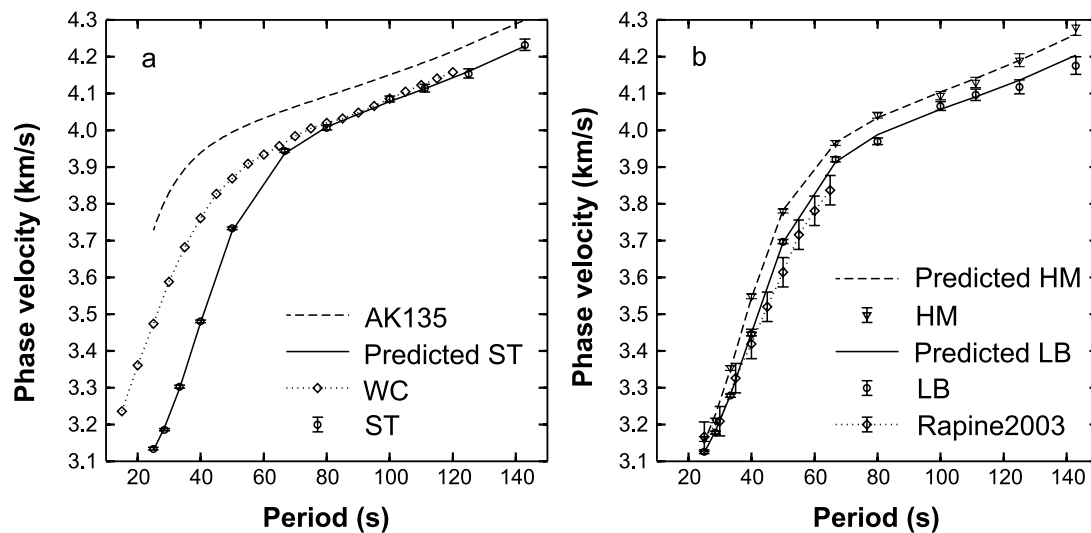


Figure 7. (a) Average Rayleigh-wave phase velocities in Southern Tibet (circles with error bars) compared with those of the global AK135 model (dashed line), and west China (dotted line with open diamonds, Yao *et al.* 2005). The solid line denotes the predicted dispersion curve in the inversion for 1-D average shear wave velocity model. (b) Average Rayleigh wave phase velocities of two tectonic provinces: the Himalayas (inverted triangles with error bars) and the Lhasa block (circles with error bars). The predicted dispersion curves of the two provinces are plotted with dashed line and solid line, respectively. A comparable result of average phase velocities of the Lhasa block (Rapine *et al.* 2003) is also plotted with dotted line with diamonds.

previous studies (Cotte *et al.* 1999; Wittlinger *et al.* 2004). Rapine *et al.* (2003) measured the average phase velocities in the Lhasa block using the data recorded by the INDEPTH III array. They measured the phase velocities at the periods shorter than 70 s by the source-station analysis. In Fig. 7(b), our results in the Lhasa block are slightly different from theirs. We think that this slight difference makes sense owing to the very different data sets and analysis approaches. First, our data have better azimuthal coverage than theirs. Second, their study region is much broader than ours. Last, the source-station method they used may cause systemic deviations because the energy of non-planar wavefields is ignored (Wielandt 1993).

With the average phase velocities as initial velocities, we have conducted the inversions for 2-D isotropic phase velocity structure at 11 frequency bands in southern Tibet. Maps of 2-D phase velocity anomalies at the periods of 25, 33, 40, 50, 67, 100, 125 and 143 s are shown in Fig. 8. Velocity anomalies are calculated relative to the average phase velocities in the entire study region. The maps are clipped with the contour of 2 per cent double standard deviations for phase velocity anomalies at the period of 50 s (Fig. 8c). The phase velocities of Rayleigh waves at the periods of 25–50 s are dominantly sensitive to the crustal structure in southern Tibet. Low velocity anomalies mainly appear in the Lhasa block, and are unevenly distributed. The low velocity zones concentrate in the regions of the N–S trending rifts (TYR and PXR). The lateral boundary between high and low velocities extends roughly in E–W direction. At the long periods of 100, 125 and 143 s, the phase velocities mainly reflect the structure of mantle lithosphere. Low velocity anomalies appear beneath the N–S trending rifts and extend southward into the Himalayas. At the same time, the low velocity anomaly beneath the PXR seems to dip eastward. The shape and distribution of phase velocity anomalies at long periods are very different from those at short periods. Particularly, the phase velocity anomalies at 67 s reflect both the lateral velocity variations and the Moho depth undulations. It is hard to extract clear information on the lithospheric structure directly.

We have run a series of checkerboard tests to check the resolution of the resultant 2-D isotropic phase velocity structure. Input velocity anomalies are ± 3 per cent relative to the average phase velocities in the entire study region. The synthetic data of amplitudes and phases are calculated based on the ray paths of real data. Gaussian random errors are added to the synthetic data before the inversions. The approach on how to produce the synthetic data and random errors is elaborated in Li *et al.* (2003). The controlling parameters in the checkerboard inversions are the same as those in the inversions with real data. The results for the checkerboard model with an anomaly size of ~ 200 km at short (25 s), intermediate (50 s) and long periods (100 s) are shown in Fig. 9. At all periods, the patterns of velocity anomalies are clearly recovered. The amplitudes of anomalies are recovered at 50 s and partly recovered at 25 and 100 s. We have also run the checkerboard tests with smaller-sized phase velocity anomalies and found that the checkerboard could hardly be recovered at long periods. The reduction of lateral resolution at short and long periods is primarily due to the lack of data coverage (Fig. 4). The improved method with finite frequency kernels is reported to be able to improve the lateral resolution at long periods (Yang & Forsyth 2006).

We have checked the fitting of wavefields in the inversions. The example event occurred at Japan arc on 2004 October 27 with $M_s = 5.4$. The Rayleigh waves propagated across the heterogeneous continent of Eastern China before arriving to the study region. The observed amplitudes and phases (Figs 10c and d) at 50 s display severe lateral heterogeneity and the energy of non-planar waves is unignorable. As expected, such a complex wavefield is able to be well fitted in the inversions (Figs 10a and c).

3.2 Shear wave velocities

By inverting the average phase velocities, we have obtained the 1-D shear wave velocity models in southern Tibet and two blocks: the Himalayas and the Lhasa block (Fig. 11). The initial model

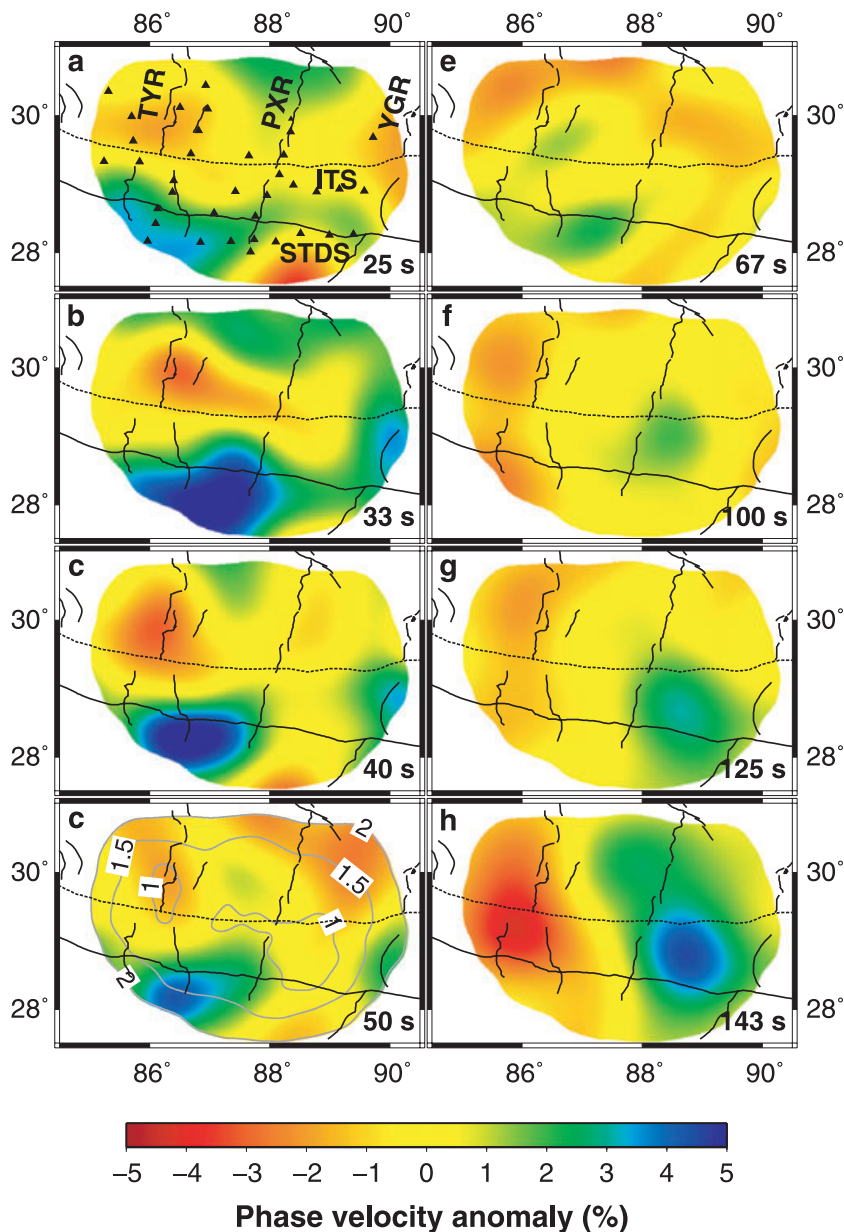


Figure 8. Maps of Rayleigh wave isotropic phase velocity anomalies and standard deviations. The phase velocity anomaly maps are illustrated at the periods of (a) 25 s, (b) 33 s, (c) 40 s, (d) 50 s, (e) 80 s, (f) 100 s, (g) 125 s and (h) 143 s. The velocity anomalies are calculated relative to the average phase velocities in the entire study region. The maps are clipped using the contour of 2 per cent double standard errors at the period of 50 s (Fig. 8d). The black triangles denote the seismic stations (Fig. 8a). The main tectonic boundaries and the N–S trending rifts are marked with the abbreviations as same as in Fig. 1.

is modified from the AK135 global model (Kennett *et al.* 1995). The initial Moho depth is 75 km for southern Tibet, 65 km for the Himalayas and 75 km for the Lhasa block according to the receiver function studies (Jin *et al.* 2006; Nabelek *et al.* 2009; Wittlinger *et al.* 2009). To check the dependence on initial models, we have repeated the inversions with different initial models. We find that the main features are consistent among the resultant models. The fitting of phase velocity data is shown in Fig. 7. Compared with the modified AK135 model, the low velocities are observed in the crust of southern Tibet, which is common for the active orogen. But the ultra-low velocity of $\sim 3.3 \text{ km s}^{-1}$ in the middle crust reflects the existence of partial melting (e.g. Brown *et al.* 1996; Kind *et al.* 1996; Nelson *et al.* 1996; Unsworth *et al.* 2005). A fast mantle lid is also identified to the depth of $\sim 160 \text{ km}$ with the shear

wave velocity of $\sim 4.7 \text{ km s}^{-1}$, which reflects the underthrusting Indian lithosphere (e.g. Kosarev *et al.* 1999; Wittlinger *et al.* 2004). The shear wave velocity in the middle crust of the Himalayas is $\sim 3.4 \text{ km s}^{-1}$ and ~ 3 per cent higher than the Lhasa block. This velocity discrepancy between two blocks is consistent with the previous studies in southern Tibet (e.g. Brown *et al.* 1996; Kind *et al.* 1996; Nelson *et al.* 1996). Decoupled with the Moho depth, the shear wave velocities in the lower crust are approximately equal for the Himalayas and the Lhasa block. The fast mantle lid is imaged to the depth of $\sim 180 \text{ km}$ in the Himalayas and $\sim 160 \text{ km}$ in the Lhasa block. The velocity discrepancy between the Himalayas and the Lhasa block is insignificant in the lower crust and mantle lithosphere. The crustal structure of the Lhasa block in this study is consistent with that from Rapine *et al.* (2003) except for the

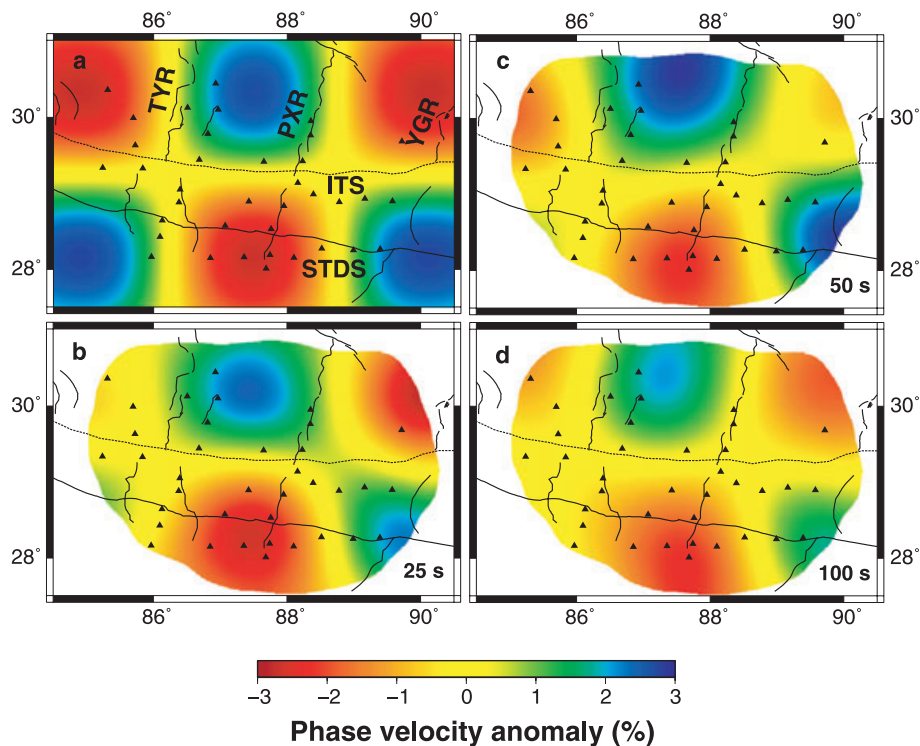


Figure 9. Checkerboard tests for the 2-D isotropic phase velocities. (a) Input model with ± 3 per cent anomaly amplitude and 200 km anomaly size. (b–d) Recovered models at short (25 s), intermediate (50 s) and long (100 s) periods. The recovered models are clipped with the same procedure as in Fig. 8(d). The black triangles denote the seismic stations. The main tectonic boundaries and the N–S trending rifts are marked with the abbreviations as same as in Fig. 1.

structure nearby the Moho. This difference is caused by the different settings in the inversions: We set a priori Moho in the velocity model, but they did not.

Rayleigh-wave phase velocities at different periods are primarily sensitive to shear wave velocities at different depths. As shown in Fig. 12(a), the sensitivity kernel at the shortest period (25 s) reaches the peak value at the depth of ~ 25 km and at the longest period (143 s) reaches the peak value at the depth of ~ 200 km. So the resultant shear wave velocity models have good depth resolution at the depths of 25–200 km. On the other hand, the sensitivity kernels at long periods become much flatter and have smaller peak values than at short periods. As a result, the resolution to shear wave velocities decreases with depth. We confirm the decreasing of resolution with depth in the model resolution matrix (Fig. 12b). The resolution to shear wave velocities at each layer peaks at the right depth, but their peak values become smaller as the depths of layers increase. There are total five pieces of independent information derived from the 1-D inversion: ~ 0.85 for shear wave velocity at the depths of 25–50 km, ~ 0.7 at the depths of 50–73 km (the Moho) and ~ 1.6 at the depths of 73–200 km. So the average velocities in the middle crust, lower crust and mantle lithosphere can be well determined.

With the same inversion procedure, we have inverted for 1-D shear wave velocity models at each node in the 2-D phase velocity model to obtain a 3-D model in southern Tibet. The lithosphere structure observed directly from phase velocities is vague and even misleading without correction for the crustal thickness (e.g. Griot *et al.* 1998). The joint inversion of shear wave velocities and crustal thickness can solve the problem, but bring in the trade-off between them. We change the initial model to the more realistic 1-D average shear wave velocity model in southern Tibet and interpolate the crustal thickness derived from the receiver function studies using the Hi-CLIMB data (Jin *et al.* 2006; Nabelek *et al.* 2009) to obtain

the initial map of crustal thickness. The crustal thickness is more heavily damped than shear wave velocities in the inversions because the initial crustal thickness is fairly accurate. The resolution of the resultant 3-D shear wave velocity model can be derived from both the lateral resolution of 2-D phase velocity inversions and the depth resolution of 1-D shear wave velocity inversions.

The resultant 3-D shear velocity model of the crust is shown in Fig. 13. The shape and distribution of shear wave velocity anomalies are remarkably different between the middle and lower crust, which reflects the existence of a decollement between the middle and lower crust (Burchfiel *et al.* 1989; Zhao *et al.* 1993; Hauck *et al.* 1998). This decollement was widely observed in southern Tibet by the previous studies (Brown *et al.* 1996; Nelson *et al.* 1996; Schulte-Pelkum *et al.* 2005; Nabelek *et al.* 2009). In the middle crust, a large low velocity anomaly appears in the Lhasa block. Such a low velocity anomaly was also imaged by INDEPTH data and interpreted as the presence of partial melting (Brown *et al.* 1996; Makovsky *et al.* 1996; Nelson *et al.* 1996; Unsworth *et al.* 2005). In the lower crust, low velocity anomalies appear along the TYR and PXR.

The resultant 3-D shear wave velocity model of the mantle lithosphere is shown in Fig. 14. The low velocity anomalies continue appearing along the N–S trending rifts in consistent with the velocity structure in the lower crust. The low velocity anomalies along the TYR and PXR can be recognized from the lower crust to the bottom of lithosphere. The similar low velocity anomalies were imaged along the N–S trending rifts in southern and southeastern Tibet (Ren & Shen 2008; Hung *et al.* 2010; Liang *et al.* 2011). The low velocity structure beneath the PXR seems to dip eastward. High velocity anomalies appear in the non-rift regions, which is consistent with the obvious interpretation that the Indian lithosphere is underthrusting beneath southern Tibet.

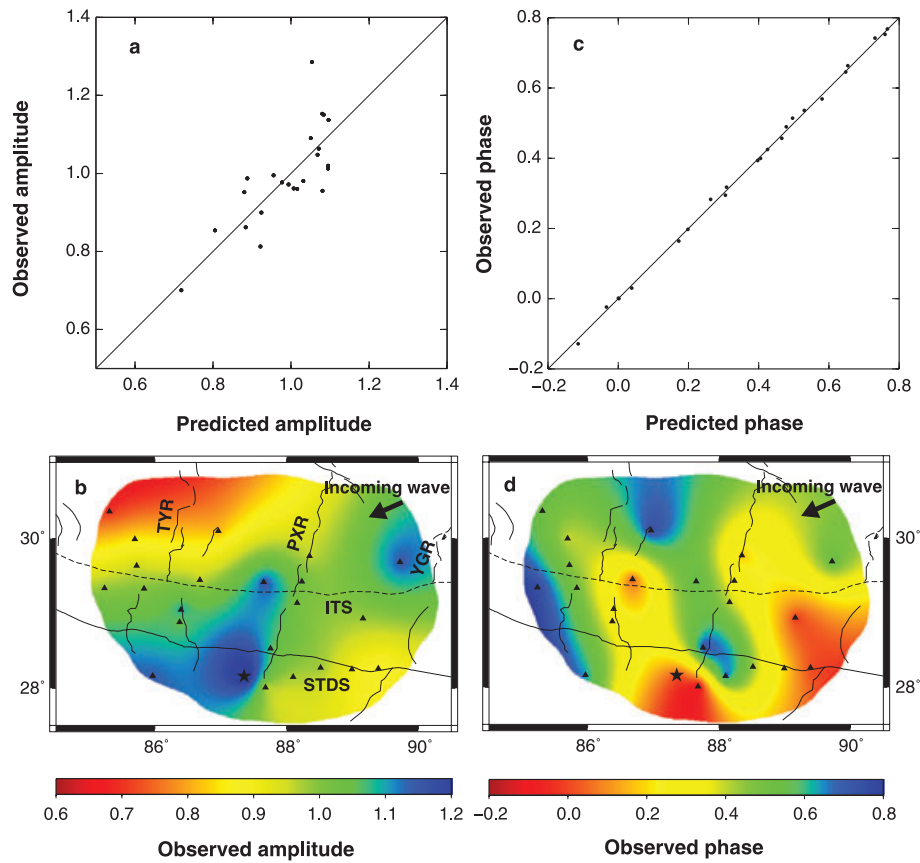


Figure 10. Fitting of the Rayleigh wavefield of the example event at the period of 50 s. The earthquake occurred at Japan arc on 2004 October 27, with $M_s = 5.4$. (a) and (c) Comparison of predicted and observed normalized amplitudes and phases in the inversion for 2-D isotropic phase velocity model. The amplitudes are normalized by the rms of the observed amplitudes. The phases are calculated relative to the phase at the reference station. (b) and (d) Maps of observed normalized amplitudes and phases. The maps are clipped with the same procedure as in Fig. 8(d). The black arrows denote the incident direction of the Rayleigh waves. 23 stations (triangles and stars) have recorded ‘good’ Rayleigh waveforms. The black stars denote the reference station with zero phases for this event.

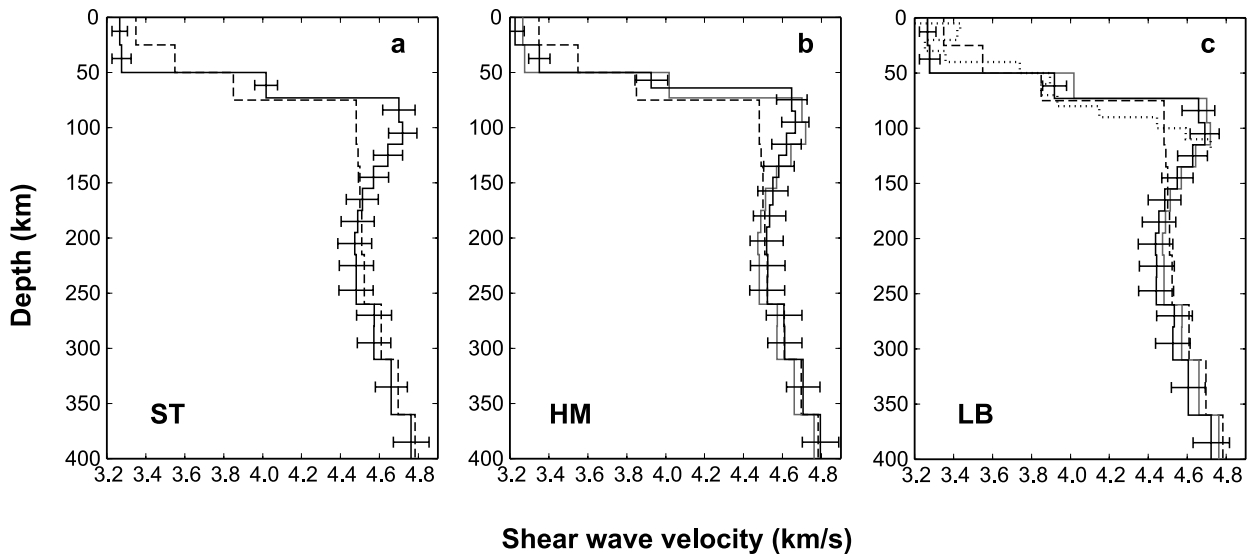


Figure 11. 1-D average shear wave velocities in (a) southern Tibet and two tectonic provinces: (b) the Himalayas and (c) the Lhasa block. The resultant shear wave velocities are plotted with solid lines with error bars. The modified AK135 global model with the crustal thickness of 75 km (Kennett *et al.* 1995) is plotted with dashed lines. The average shear wave velocities in southern Tibet are plotted with grey solid lines in Fig. 11(b) and (c) for comparison. Another shear wave velocity model in the Lhasa block (Rapine *et al.* 2003) is shown with dotted line in Fig. 11(c).

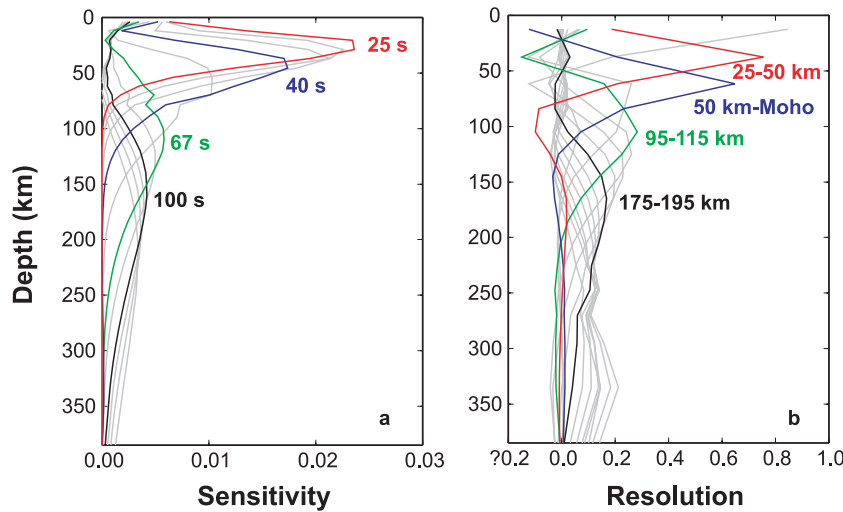


Figure 12. (a) Rayleigh wave phase velocity sensitivity kernels to the 1-D average shear wave velocity model in southern Tibet. The kernel at the shortest period (25 s) has a peak sensitivity of ~ 25 km and at the longest period (143 s) has a peak sensitivity of ~ 200 km. (b) Rows of the resolution matrix for the average shear wave velocity model in southern Tibet. The resolution for each layer corresponds to one row of the matrix and is plotted with a curve. The sharper the peak is, the higher the resolution is for that layer.

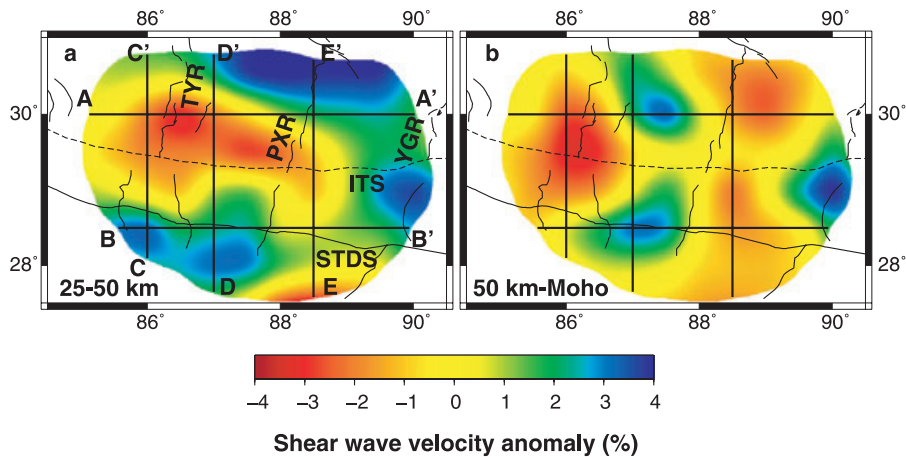


Figure 13. Maps of shear wave velocity anomalies in the crust: (a) 25–50 km and (b) 50 km–Moho. The velocity anomalies are calculated relative to the average shear wave velocity in southern Tibet. The maps are clipped with the same procedure as in Fig. 8(d). The main tectonic boundaries and the N–S trending rifts are marked with the abbreviations as same as in Fig. 1. Locations of vertical profiles are plotted either.

Four vertical profiles are presented in Fig. 15 to highlight the differences among these rifts and between rifts and non-rift regions. The profiles A–A' and B–B' situate in the Lhasa block and the Himalayas, respectively. They extend across the TYR and PXR from west to east. The profiles C–C' and E–E' run along the TYR and PXR, respectively and the profile D–D' is in the non-rift regions between them. The E–W trending profiles (A–A' and B–B') show prominent low velocity anomalies along the TYR and PXR from the lower crust to mantle lithosphere. The lower boundary of the low velocity anomaly along the TYR is beyond 200 km deep, while the low velocity anomaly along the PXR terminates at the depth of ~ 150 km or dips eastward. We cannot make a conclusion which state is real because of the lateral smearing at that depth. The N–S trending profiles (C–C', D–D' and E–E') show a clear structural contrast between rifts and non-rift regions. The low velocity anomalies beneath the rifts are uninterrupted from the lower crust to the mantle lithosphere and from the Himalayas to the Lhasa block. A slab-like high velocity anomaly is observed across southern Tibet beneath the non-rift regions.

4 DISCUSSIONS

4.1 Crustal Channel flow in southern Tibet

Observations of coincident low seismic velocity anomalies (Kind *et al.* 1996; Nelson *et al.* 1996; Hung *et al.* 2010), low electric resistivity (Pham *et al.* 1986; Chen *et al.* 1996; Wei *et al.* 2001; Unsworth *et al.* 2005), reflection bright spots (Brown *et al.* 1996; Makovsky *et al.* 1996) and high heat flow (Francheteau *et al.* 1984) in southern Tibet all attest to the presence of partial melt and/or aqueous fluids in the middle and/or lower crust. These observations are commonly interpreted as strong evidences for southward crustal channel flow (Beaumont *et al.* 2001, 2004; Unsworth *et al.* 2005). The notion of crustal channel flow is very popular to explain the E–W extension of central and eastern Tibet (e.g. Clark & Royden 2000; Royden *et al.* 2008). But whether the channel flow exists in southern Tibet or not and how it distributes are controversial (Chung *et al.* 2005; Hung *et al.* 2010).

Our results show a pervasive low shear wave velocity anomaly in the middle crust of the Lhasa block (Fig. 13a), which covers

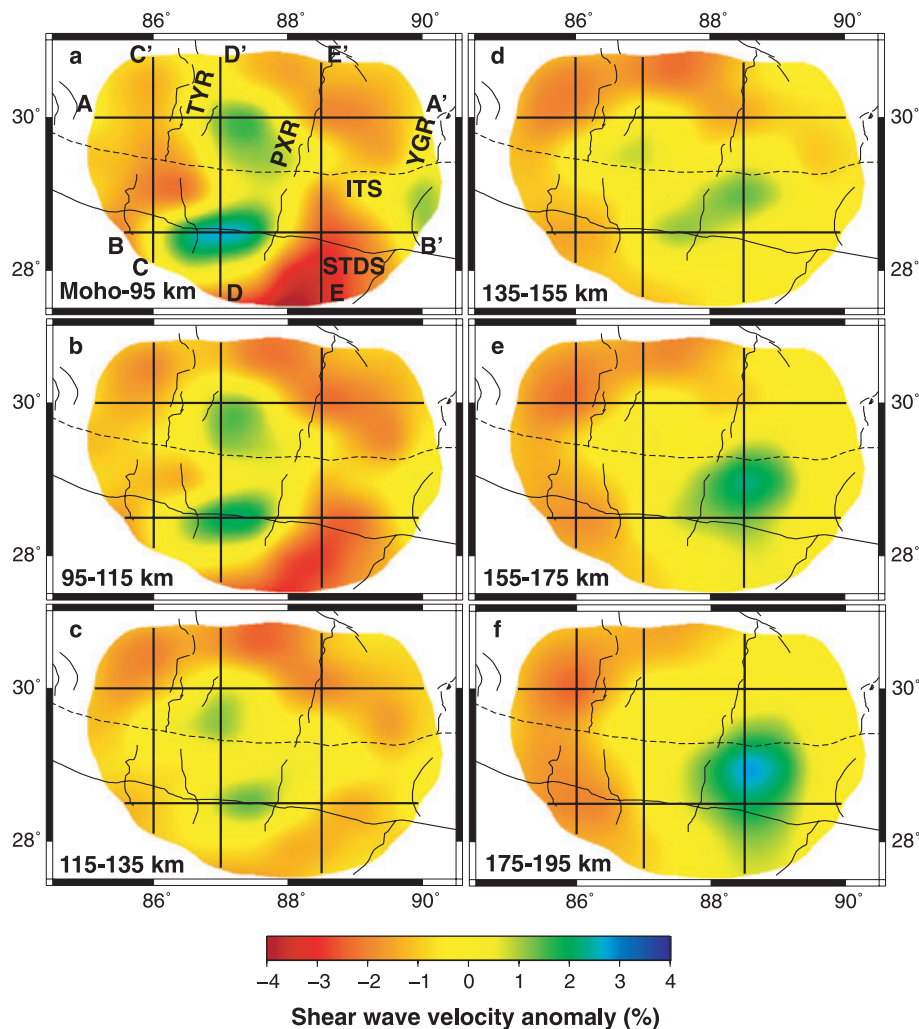


Figure 14. Maps of shear wave velocity anomalies in the mantle: (a) Moho–95 km, (b) 95–115 km, (c) 115–135 km, (d) 135–155 km, (e) 155–175 km and (f) 175–195 km. The velocity anomalies are calculated relative to the average shear wave velocity in southern Tibet. The maps are clipped with the same procedure as in Fig. 8(d). The main tectonic boundaries and the N–S trending rifts are marked with the abbreviations as same as in Fig. 1. Locations of vertical profiles are plotted either.

the N–S trending rifts and non-rift regions. But the low velocity anomalies along the rifts in the lower crust are not interconnected (Fig. 13b), which is consistent with the observation of Hung *et al.* (2010). The very different structures in the middle and lower crust are not artificial because they can also be recognized from the 2-D phase velocity anomaly models (Fig. 8). The INDEPTH geophysical investigations (e.g. Nelson *et al.* 1996; Unsworth *et al.* 2005) suggested a wholesale channel flow model in the middle crust. But both their seismic and magnetotelluric profiles are along the N–S trending rifts and provide no constrains on the structure of non-rift regions. Hung *et al.* (2010) argued that the wholesale crustal channel flow model is untenable because their 3-D body wave tomography results indicated that the low velocity anomalies in the lower crust concentrated beneath the rifts and were not interconnected. Our results reconcile the wholesale crustal channel flow model proposed by the INDEPTH projects and the 3-D tomography results of Hung *et al.* (2010), and support the pervasive mid-crustal channel flow in southern Tibet.

Seismic tomography can only provide constrains on the current status of the lithosphere in southern Tibet. The observed low velocity anomaly in the middle crust does not corroborate the presence

of Miocene channel flow in the middle crust. The emplacement of Himalayan leucogranites, and rapid exhumation and metamorphism along the southernmost Tethyan Himalayas are usually attributed to the Miocene crustal channel flow (Zeitler *et al.* 2001; Beaumont *et al.* 2004). But studies on the Miocene magmatism in the Lhasa block indicated the widespread occurrence of ultrapotassic and adakitic magmatism, which were interpreted as melts of the metasomatized lithospheric mantle and mafic lower crust, respectively (Williams *et al.* 2001; Chung *et al.* 2005). If it existed, the Miocene channel flow would be likely to occur in the lower crust and be very different from the current channel flow in the middle crust.

4.2 N–S trending rifts in southern Tibet

The geological history of the salient N–S trending rifts in southern Tibet, which relate to Cenozoic E–W extension of the plateau, has been a puzzle for more than three decades (Taylor & Yin 2009). Previous studies tended to the explanation that the rifts in southern Tibet were restricted only to the upper crust, based on the analysis of rift flank topography (Masek *et al.* 1994) and geophysical observations (Cogan *et al.* 1998; Nelson *et al.* 1996). To the contrary, Instability

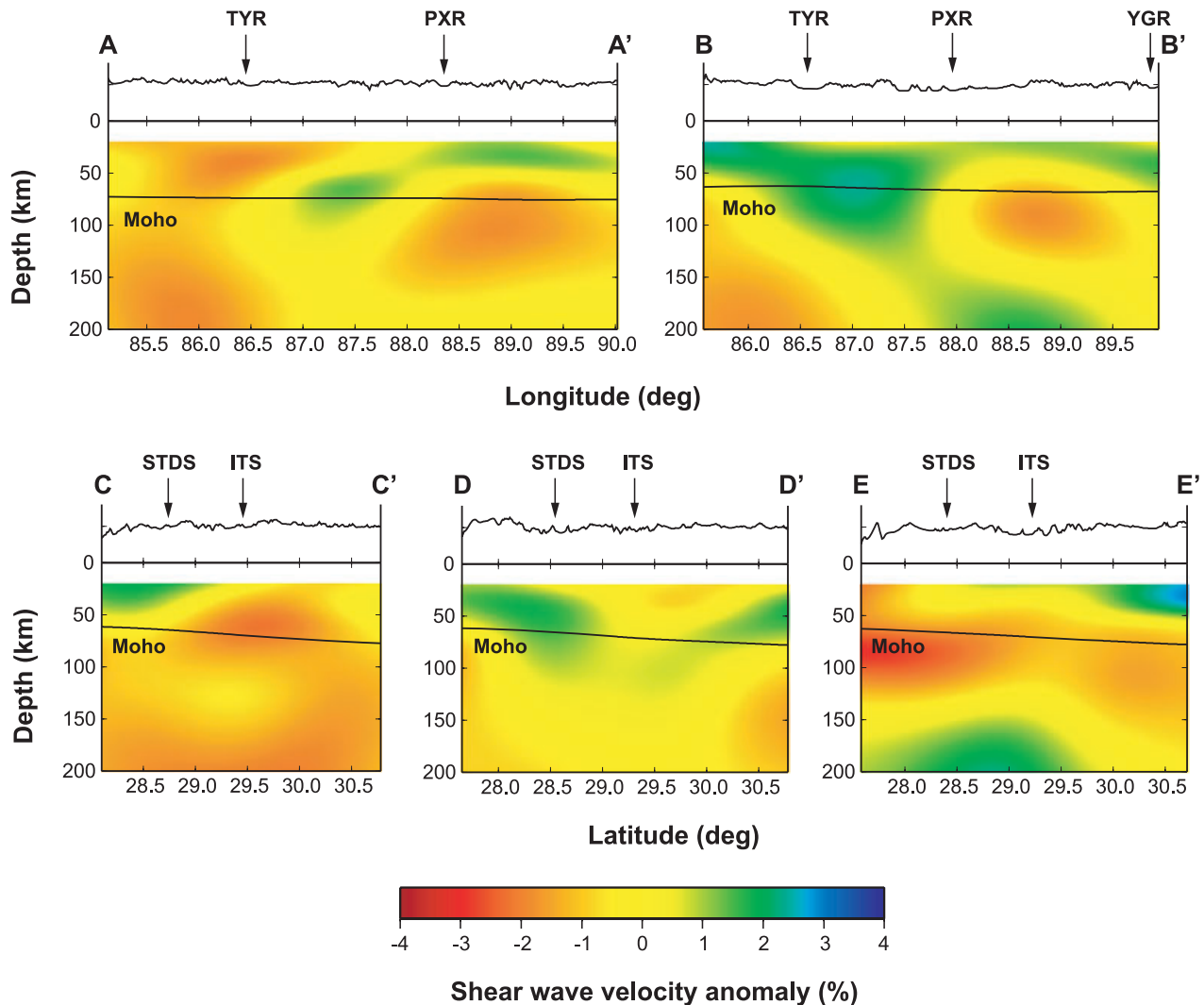


Figure 15. Vertical profiles of shear wave velocity anomalies. Profiles A–A' and B–B' are along latitude 30°N and 28.5°N. Profiles C–C', D–D' and E–E' are along longitude 86°E, 87°E and 88.5°E. Locations of these profiles are shown in Figs 13 and 14. The velocity anomalies are calculated relative to the average shear wave velocity in southern Tibet. Topography and Moho are plotted above and in the velocity anomaly profiles. The main geological boundaries and the N–S trending rifts are marked with the abbreviations as same as in Fig. 1.

analysis based on rift spacing requires a coherent E–W extension throughout the entire crust and mantle lithosphere (Yin 2000). Focal depths and mechanisms of the earthquakes directly beneath the rifts further suggest the brittle E–W extension are accommodated by both the upper crust and the upper mantle (Chen & Molnar 1983; Zhu & Helmlberger 1996; Chen & Yang 2004). Furthermore, recent body wave tomography studies provided direct contrary evidences, that low velocity anomalies from the lower crust to the mantle lithosphere were imaged along the rifts (Ren & Shen 2008; Hung *et al.* 2010; Liang *et al.* 2011). The conflict observations also occur in our results. Both the pervasive low velocity anomaly in the middle crust and the difference of the shape and distribution of velocity anomalies between the middle and lower crust reflect the presence of structure decoupling in the crust of southern Tibet (Fig. 13). This decoupling leads to the conclusion that the N–S trending rifts are restricted in the upper crust. While the low velocity anomalies from the lower crust to the mantle lithosphere along the TYR and the PXR argue that the formation of these rifts is associated with the entire lithosphere (Figs 13–15). The paradoxical implications on the N–S trending rifts reflect that the formation of the rifts is a

complicated multistage tectonic process, which is supported by the recent geological investigation (Kapp *et al.* 2008).

Comparison of igneous activity and age of onset of rifting in southern Tibet may provide some insights on this multistage tectonic process. Geochemical and geochronological studies on the igneous rocks in southern Tibet suggested the Miocene ultrapotassic and adakitic magmatism (~26 to 10 Ma) was nearly coeval with onset of the E–W extension (Williams *et al.* 2004; Chung *et al.* 2005). They also found that the magma dyke swarms were often associated with the N–S trending rifts (Williams *et al.* 2001). Local asthenospheric upwelling is implied from the presence of ultrapotassic and adakitic magmas along the rifts, which originate from the mantle lithosphere and the lower crust, and leads to the break of the entire lithosphere along the rifts in southern Tibet at ~26–10 Ma. The starting age of the N–S trending rifts in southern Tibet is usually constrained to be later than ~8 Ma (Harrison *et al.* 1995; Yin *et al.* 1999; Maheo *et al.* 2007). The age discrepancy between the onset of rifting and the Miocene magmatism denies the simple model that the N–S trending rifts are formed though a coherent deformation throughout the entire lithosphere. We present a possible scenario as follows: In

the early stage (~26–10 Ma), the Miocene magmatism broke the entire lithosphere along the N–S trending rifts. The rifts initiated with the coherent rifting throughout the entire lithosphere. In the late stage (after ~8 Ma), the occurrence of partial melting in the middle crust destroyed the coherent rifting throughout the lithosphere. The rifting continued and was restricted in the upper crust. The current N–S trending rifts in southern Tibet are decoupled with the lower crust and mantle lithosphere because of the wholesale mid-crustal channel flow derived from this study as well as the previous studies (e.g. Nelson *et al.* 1996; Unsworth *et al.* 2005). The geological history of these rifts is yet close associated with the deformation or break of the entire lithosphere.

4.3 The Indian lithosphere beneath the Tibet

There is no doubt that the shape of the Indian lithosphere beneath the Tibet plays a key role in the tectonic evolution of the plateau. Recent studies using the data acquired from the Hi-CLIMB array indicated that the subhorizontally underthrusting Indian mantle lithosphere reached ~100 km north of the BNS (~33°N, Chen *et al.* 2010; Hung *et al.* 2010) and the underthrusting Indian lower crust slid to ~31°N (Nabelek *et al.* 2009). Furthermore, the underthrusting of the Indian lithosphere is along distributed evolving subparallel structures (Nabelek *et al.* 2009; Liang *et al.* 2011). Our results show no constrains on these interior boundaries because of the limitation of the study region and the inherence of surface waves. But the presence of a slab-like high velocity anomaly in the non-rift regions (Fig. 15), which can be traced from the Himalayas to the Lhasa block, is consistent with the implication of a subhorizontally underthrusting Indian lithosphere. On the other hand, the presence of low velocity anomalies from the lower crust to the mantle lithosphere along the N–S trending rifts in this study as well as in the recent studies (Ren & Shen 2008; Hung *et al.* 2010; Liang *et al.* 2011) suggests that the underthrusting Indian lithosphere has been broken into pieces during the E–W extension of the plateau. As a corollary, we conclude that the central part (~85°E–90°E) of southern Tibet is now underlain by the broken Indian lower crust and mantle lithosphere.

5 CONCLUSIONS

We have carried out the Rayleigh-wave tomography in southern Tibet with the data recorded by a 2-D seismic array, which is a part of the Hi-CLIMB array. A 3-D shear wave velocity model is established for the lithosphere structure in southern Tibet.

A pervasive low shear wave velocity anomaly is observed in the middle crust of the Lhasa block, which supports the wholesale mid-crustal channel flow in southern Tibet. Previous evidences for the mid-crustal channel flow were derived from the seismic and magnetotelluric profiles along the N–S trending rifts (e.g. Nelson *et al.* 1996; Unsworth *et al.* 2005). Our results confirm the presence of low velocity anomalies in the middle crust of non-rift regions. In the lower crust, low shear wave velocity anomalies are observed along the TYR and PXR. The shape and distribution of velocity anomalies are remarkably different between the middle and lower crust, which reflects the structural decoupling between the middle and lower crust.

The low shear wave velocity anomalies along the TYR and PXR are imaged from the lower crust to the bottom of lithosphere and from the Himalayas to the Lhasa block. The lower boundary of the low velocity anomaly beneath the TYR is beyond 200 km deep,

while the low velocity anomaly beneath the PXR terminates at the depth of ~150 km or dips eastward. A simple rifting model cannot interpret the current coexistence of (1) the structural decoupling between the middle and lower crust and (2) the low velocity anomalies from the lower crust to the mantle lithosphere beneath the N–S trending rifts. We propose that the rifting along the N–S trending rifts is a coherent deformation throughout the entire lithosphere in the early stage and then decoupled with the lower crust and mantle lithosphere in the late stage. The current N–S trending rifts in southern Tibet are restricted in the upper crust.

In the non-rift regions, a slab-like high velocity anomaly is identified beneath both the Himalayas and the Lhasa block, which is interpreted as the underthrusting Indian lithosphere. Together with the observations of low velocity anomalies along the TYR and PXR, we suggest the central part of southern Tibet is now underlain by the broken Indian lower crust and mantle lithosphere.

ACKNOWLEDGMENTS

We thank John Nabelek and his HI-CLIMB field team for their hard work at the southern Tibet to collect the data used in this study. We thank Eric Sandvol and Yingjie Yang for applying the tomography codes. We also thank three anonymous reviewers for their constructive comments, which improve the manuscript. All figures in this paper were plotted with the Generic Mapping Tools (Wessel, P. & Smith, W.H.F.). This study is funded by Natural science fundation of China (grant number: 40774017 and 40904022). Mingming Jiang acknowledges China Scholarship Council supported the study trip to United States.

REFERENCES

- Argand, E., 1924. La Tectonique de l'Asie. in *Compte-rendu du 13e congrès Géologique International*, pp. 171–372, Vaillant-Carmann, Liège.
- Armijo, R., Tapponnier, P., Mercier, J.P. & Han, T., 1986. Quaternary extension in southern Tibet, *J. geophys. Res.*, **91**, 13803–13872.
- Armijo, R., Tapponnier, P. & Han, T., 1989. Late Cenozoic right-lateral strike-slip faulting across southern Tibet, *J. geophys. Res.*, **94**, 2787–2838.
- Beaumont, C., Jamieson, R.A., Nguyen, M.H. & Lee, B., 2001. Himalayan tectonics explained by extrusion of a low-viscosity channel coupled to focused surface denudation, *Nature*, **414**, 738–742.
- Beaumont, C., Jamieson, R.A., Nguyen, M.H. & Medvedev, S., 2004. Crustal channel flows: 1. Numerical models with applications to the tectonics of the Himalayan-Tibetan orogen, *J. geophys. Res.*, **109**, B06406, doi:10.1029/2003JB002809.
- Besse, J., Courtillot, V., Pozzi, J.P., Westphal, M. & Zhou, Y.X., 1984. Paleomagnetic estimates of crustal shortening in the Himalayan Thrusts and Zangbo Suture, *Nature*, **311**, 621–626.
- Brown, L.D. *et al.*, 1996. Bright spots, structure, and magmatism in southern Tibet from INDEPTH seismic reflection profiling, *Science*, **274**, 1688–1690.
- Burchfiel, B.C., Deng, Q., Molnar, P., Royden, L.H., Wang, Y., Zhang, P. & Zhang, W., 1989. Intracrustal detachment with zones of continental deformation, *Geology*, **17**, 748–752.
- Chen, W.-P. & Molnar, P., 1983. Focal depths of intracontinental and intraplate earthquakes and their implications for the thermal and mechanical properties of the lithosphere, *J. geophys. Res.*, **88**, 4183–4214.
- Chen, W.-P. & Yang, Z., 2004. Earthquakes beneath the Himalayas and Tibet: evidence for strong lithospheric mantle, *Science*, **304**, 1949–1952, doi:10.1126/science.1097324.
- Chen, L.H., Booker, J.R., Jones, A.G., Wu, N., Unsworth, M.J., Wei, W.B. & Tan, H.D., 1996. Electrically conductive crust in southern Tibet from INDEPTH magnetotelluric surveying, *Science*, **274**, 1694–1696.

- Chen, W.-P., Martin, M., Tseng, T.-L., Nowack, R.L., Hung, S.-H. & Huang, B.-S., 2010. Shear-wave birefringence and current configuration of converging lithosphere under Tibet, *Earth planet. Sci. Lett.*, **295**, 297–304.
- Chung S.-L. *et al.*, 2005. Tibetan tectonic evolution inferred from spatial and temporal variations in post-collisional magmatism, *Earth Sci. Rev.*, **68**, 173–196.
- Clark, M.K. & Royden, L.H., 2000. Topographic ooze: building the eastern margin of Tibet by lower crustal flow, *Geology*, **28**, 703–706.
- Cogan, M.J., Nelson, K.D., Kidd, W.S.F., Wu, C. & Project INDEPTH Team, 1998. Shallow structure of the Yadong-Gulu rift, southern Tibet, from refraction analysis of Project INDEPTH common midpoint data, *Tectonics*, **17**, 46–61.
- Cotte, N., Pedersen, H., Campillo, M., Mars, J., Ni, J.F., Kind, R., Sandvol, E. & Zhao, W., 1999. Determination of the crustal structure in southern Tibet by dispersion and amplitude analysis of Rayleigh waves, *Geophys. J. Int.*, **138**, 809–819.
- DeCelles, P.G., Robinson, D.M. & Zandt, G., 2002. Implications of shortening in the Himalayan fold-thrust belt for uplift of the Tibetan Plateau, *Tectonics*, **21**, 1062, doi:10.1029/2001TC001322.
- Dewey, J.F. & Burke, K.C.A., 1973. Tibetan, Variscan, and Precambrian basement reactivation—products of continental collision, *J. Geol.*, **81**, 683–692.
- England, P. & Houseman, G., 1989. Extension during continental convergence, with application to the Tibetan Plateau, *J. geophys. Res.*, **94**, 17561–17579.
- Forsyth, D.W. & Li, A., 2005. Array analysis of two-dimensional variations in surface wave phase velocity and azimuthal anisotropy in the presence of multipathing interference. in *Seismic Earth; Array Analysis of Broadband Seismograms*, pp. 81–97, eds Levander, A. & Nolet, G. American Geophysical Union, Washington, DC.
- Francheteau, J., Jaupart, C., Shen, X.J., Kang, W.H., Lee, D.L., Bai, J.C., Wei, H.P. & Deng, H.Y., 1984. High heat-flow in southern Tibet, *Nature*, **307**, 32–36.
- Friederich, W., 2003. The S-velocity structure of the East Asian mantle from inversion of shear and surface waveforms, *Geophys. J. Int.*, **153**, 88–102.
- Griot, D.K., Montagner, J.P. & Tapponnier, P., 1998. Phase velocity structure from Rayleigh and Love waves in Tibet and its neighboring regions, *J. geophys. Res.*, **103**, 21215–21232.
- Harrison, T.M., Copeland, P., Kidd, W.S.F. & Lovera, O., 1995. Activation of the Nyainqentanghla shear zone: implications for uplift of the southern Tibetan Plateau, *Tectonics*, **14**, 658–676.
- Hauck, M.L., Nelson, K.D., Brown, L.D., Zhao, W.J. & Ross, A.R., 1998. Crustal structure of the Himalayan orogen at similar to 90° east longitude from Project INDEPTH deep reflection profiles, *Tectonics*, **17**, 481–500.
- Hoke, L., Lamb, S., Hilton, D.R. & Poreda R.J., 2000. Southern limit of mantle-derived geothermal helium emissions in Tibet: implications for lithospheric structure, *Earth planet. Sci. Lett.*, **180**, 297–308.
- Hung, S.-H., Chen, W.-P., Chiao, L.-Y. & Tseng, T.-L., 2010. First multi-scale, finite-frequency tomography illuminates 3-D anatomy of the Tibetan Plateau, *Geophys. Res. Lett.*, **37**, L06304, doi:10.1029/2009GL041875.
- Jin, G. *et al.*, 2006. Receiver function images of the crust and upper mantle structure of southern Tibet, *EOS, Trans. Am. geophys. Un.*, **87**, Fall Meet. Suppl., Abstract T53F-04.
- Johnson, M.R.W., 2002. Shortening budgets and the role of continental subduction during the India-Asia collision, *Earth Sci. Rev.*, **59**, 101–123.
- Kapp, P., Taylor, M., Stockli, D. & Ding, L., 2008. Development of active low-angle normal fault systems during orogenic collapse: Insight from Tibet, *Geology*, **36**, 7–10, doi:10.1130/G24054A.1.
- Kennett, B.L.N., Engdahl, E.R. & Buland, R., 1995. Constraints on seismic velocities in the Earth from travel-times, *Geophys. J. Int.*, **122**, 108–124.
- Kind, R. *et al.*, 1996. Evidence from earthquake data for a partially molten crustal layer in southern Tibet, *Science*, **274**, 1692–1694.
- Kosarev, G., Kind, R., Sobolev, S.V., Yuan, X., Hanka, W. & Oreshin, S., 1999. Seismic evidence for a detached Indian lithospheric mantle beneath Tibet, *Science*, **283**, 1306–1309.
- Li A. & Burke, K., 2006. Upper mantle structure of southern Africa from Rayleigh wave tomography, *J. geophys. Res.*, **111**, B10303, doi:10.1029/2006JB004321.
- Li, A.B., Forsyth, D.W. & Fischer, K.M., 2003. Shear velocity structure and azimuthal anisotropy beneath eastern North America from Rayleigh wave inversion, *J. geophys. Res.*, **108**, 2362, doi:10.1029/2002JB002259.
- Li C., Van Der Hilst, R.D., Meltzer, A.S. & Engdahl, E.R., 2008. Subduction of the Indian lithosphere beneath the Tibetan Plateau and Burma, *Earth planet. Sci. Lett.*, **274**, 157–168, doi:10.1016/j.epsl.2008.07.016.
- Liang, X. *et al.*, 2008. Earthquake distribution in southern Tibet and its tectonic implications, *J. geophys. Res.*, **113**, B12409, doi:10.1029/2007JB005101.
- Liang, X., Shen, Y., Chen, Y.J. & Ren, Y., 2011. Crustal and mantle velocity models of southern Tibet from finite frequency tomography, *J. geophys. Res.*, **116**, B02408, doi:10.1029/2009JB007159.
- Liu, M. & Yang, Y., 2003. Extensional collapse of the Tibetan Plateau: results of three-dimensional finite element modeling, *J. geophys. Res.*, **108**(B8), 2361, doi: 10.1029/2002JB002248.
- Maheo, G. *et al.*, 2007. Post 4 Ma initiation of normal faulting in southern Tibet. Constraints from the Kung Co half graben, *Earth planet. Sci. Lett.*, **256**, 233–243.
- Makovsky, Y., Klemperer, S.L., Ratschbacher, L., Brown, L.D., Li, M., Zhao, W.J. & Meng, F.L., 1996. INDEPTH wide-angle reflection observation of P-wave-to-S-wave conversion from crustal bright spots in Tibet, *Science*, **276**, 1690–1691.
- Masek, J.G., Isacks, B.L., Fielding, E.J. & Browaeys, J., 1994. Rift flank uplift in Tibet: Evidence for a viscous lower crust, *Tectonics*, **13**, 659–667.
- McCaffery, R. & Nabelek, J., 1998. Role of oblique convergence in the active deformation of the Himalayas and southern Tibet plateau, *Geology*, **26**, 691–694.
- Mitchell, B.J., 1995. Anelastic structure and evolution of the continental crust and upper mantle from seismic surface wave attenuation, *Rev. Geophys.*, **33**, 441–462.
- Molnar, P. & Tapponnier, P., 1975. Cenozoic tectonics of Asia—effects of a continental collision, *Science*, **189**, 419–426.
- Molnar, P. & Tapponnier, P., 1978. Active tectonics of Tibet, *J. geophys. Res.*, **83**, 5361–5375.
- Monsalve, G., Sheehan, A., Schulte-Pelkum, V., Rajaure, S., Pandey, M.R. & Wu, F., 2006. Seismicity and one-dimensional velocity structure of the Himalayan collision zone: earthquakes in the crust and upper mantle, *J. geophys. Res.*, **111**, B10301, doi:10.1029/2005JB004062.
- Nabelek, J. *et al.*, 2009. Underplating in the Himalaya-Tibet collision zone revealed by the Hi-CLIMB experiment, *Science*, **325**, 1371, doi:10.1126/science.1167719.
- Nelson, K.D. *et al.*, 1996. Partially molten middle crust beneath southern Tibet: synthesis of project INDEPTH results, *Science*, **274**, 1684–1688.
- Ni, J. & Barazangi, M., 1984. Seismotectonics of the Himalayan collision zone—geometry of the underthrusting Indian plate beneath the Himalaya, *J. geophys. Res.*, **89**, 1147–1163.
- Owens, T.J., Randall, G.E., Wu, F.T. & Zeng, R.S., 1993. Passcal Instrument performance during the Tibetan Plateau Passive Seismic Experiment, *Bull. seism. Soc. Am.*, **83**, 1959–1970.
- Patriat, P. & Achache, J., 1984. India Eurasia collision chronology has implications for crustal shortening and driving mechanism of plates, *Nature*, **311**, 615–621.
- Pham, V.N., Boyer, D., Therme, P., Yuan, X.C., Li, L. & Jin, G.Y., 1986. Partial melting zones in the crust in southern Tibet from magnetotelluric results, *Nature*, **319**, 310–314.
- Powell, C.M. & Conaghan, P.J., 1975. Tectonic models of Tibetan plateau, *Geology*, **3**, 727–731.
- Rapine, R., Tilmann, F., West, M., Ni, J. & Rodgers, A., 2003. Crustal structure of northern and southern Tibet from surface wave dispersion analysis, *J. geophys. Res.*, **108**, 2120, doi:10.1029/2001JB000445.
- Ren, Y. & Shen, Y., 2008. Finite frequency tomography in southeastern Tibet: evidence for the causal relationship between mantle lithosphere delamination and the north-south trending rifts, *J. geophys. Res.*, **113**, B10316, doi:10.1029/2008JB005615.

- Rodgers, A.J. & Schwartz, S.Y., 1998. Lithospheric structure of the Qiangtang Terrane, northern Tibetan Plateau, from complete regional waveform modeling: evidence for partial melt, *J. geophys. Res.*, **103**, 7137–7152.
- Ross, A.R., Brown, L.D., Pananont, P., Nelson, K.D., Klempere, S., Haines, S., Zhao, W.J. & Guo, J.R., 2004. Deep reflection surveying in central Tibet: lower-crustal layering and crustal flow, *Geophys. J. Int.*, **156**, 115–128.
- Rothery, D.A. & Drury, S.A., 1984. The neotectonics of the Tibetan plateau, *Tectonics*, **3**, 19–26.
- Royden, L.H., Burchfiel, B.C. & van de Hilst, R.D., 2008. The geological evolution of the Tibetan plateau, *Science*, **321**, 1054, doi:10.1126/science.1155371.
- Saito, M., 1988. DISPER80: a subroutine package for the calculation of seismic normal-mode solution, in *Seismological Algorithms: Computational Methods and Computer Programs*, pp. 293–319, ed. Doornbos, D.J., Elsevier, New York, NY.
- Schulte-Pelkum, V., Monsalve, G., Sheehan, A., Pandey, M.R., Sapkota, S., Bilham, R. & Wu, F., 2005. Imaging the Indian subcontinent beneath the Himalaya, *Nature*, **435**, 1222–1225.
- Smith, M.L. & Dahlen, F.A., 1973. Azimuthal dependence of Love and Rayleigh-wave propagation in a slightly anisotropic medium, *J. geophys. Res.*, **78**, 3321–3333.
- Tapponnier, P. & Molnar, P., 1977. Active faulting and tectonics in China, *J. geophys. Res.*, **82**, 2905–2930.
- Tapponnier, P., Mercier, J.L., Armijo, R., Han, T. & Zhao, J., 1981. Field evidence for active normal faulting in Tibet, *Nature*, **294**, 410–414.
- Tapponnier, P., Xu, Z., Roger, F., Meyer, B., Arnaud, N., Wittlinger, G. & Yang, J., 2001. Oblique stepwise rise and growth of the Tibetan Plateau, *Science*, **294**, 1671–1677.
- Tarantola, A. & Valette, B., 1982. Generalized non-linear problems solved using the least-squares criterion, *Rev. Geophys.*, **20**, 219–232.
- Taylor, M. & Yin, A., 2009. Active structures of the Himalayan-Tibetan orogen and their relationships to earthquake distribution, contemporary strain field, and Cenozoic volcanism, *Geosphere*, **5**(3), 199–214, doi:10.1130/GES00217.1
- Tilmann, F., Ni, J. & INDEPTH III Seismic Team, 2003. Seismic imaging of the downwelling Indian lithosphere beneath central Tibet, *Science*, **300**, 1424–1427.
- Toksoz, M.N. & Bird, P., 1977. Formation and evolution of marginal basins and continental plateaus. in *Island Arcs, Deep Sea Trenches and Back-Arc Basins*, pp. 379–393, eds Talwani, M. & Pitman, W. C., American Geophysical Union, Washington, D.C.
- Unsworth, M.J., Jones, A.G., Wei, W., Marquis, G., Gokarn, S.G., Spratt, J.E. & the INDEPTH-MT team, 2005. Crustal rheology of the Himalaya and southern Tibet inferred from magnetotelluric data, *Nature*, **438**, 78–81, doi:10.1038/nature04154.
- Vergne, J., Wittlinger, G., Hui, Q.A., Tapponnier, P., Poupinet, G., Jiang, M., Herquel, G. & Paul, A., 2002. Seismic evidence for stepwise thickening of the crust across the NE Tibetan plateau, *Earth planet. Sci. Lett.*, **203**, 25–33.
- Wang, Q. *et al.*, 2001. Present-day crustal deformation in China constrained by Global Positioning System measurements, *Science*, **294**, 574–577.
- Weeraratne, D.S., Forsyth, D.W., Fischer, K.M. & Nyblade, A.A., 2003. Evidence for an upper mantle plume beneath the Tanzanian craton from Rayleigh wave tomography, *J. geophys. Res.*, **108**, 2427, doi:10.1029/2002JB002273.
- Wei, W.B. *et al.*, 2001. Detection of widespread fluids in the Tibetan crust by magnetotelluric studies, *Science*, **292**, 716–718.
- Wielandt, E., 1993. Propagation and structural interpretation of non-plane waves, *Geophys. J. Int.*, **113**, 45–53.
- Williams, H.M., Turner, S.P., Kelley, S.P. & Harris, N.B.W., 2001. Age and composition of dikes in southern Tibet: new constraints on the timing of east-west extension and its relationship to postcollisional volcanism, *Geology*, **29**, 339–342.
- Williams, H.M., Turner, S.P., Pearce, J.A., Kelley, S.P. & Harris, N.B.W., 2004. Nature of the source regions for post-collisional, potassic magmatism in southern and northern Tibet from geochemical variations and inverse trace element modeling, *J. Petrol.*, **45**, 555–607, doi:10.1093/petrology/egg094.
- Wittlinger, G., Farra, V. & Vergne, J., 2004. Lithospheric and upper mantle stratifications beneath Tibet: new insights from Sp conversions, *Geophys. Res. Lett.*, **31**, L19615, doi:10.1029/2004GL020955.
- Wittlinger, G. *et al.*, 1996. Seismic tomography of northern Tibet and Kunlun: evidence for crustal blocks and mantle velocity contrast, *Earth planet. Sci. Lett.*, **139**, 263–279.
- Wittlinger, G., Farra, V., Hetenyi, G., Vergne, J. & Nabelek, J., 2009. Seismic velocities in Southern Tibet lower crust: a receiver function approach for eclogite detection, *Geophys. J. Int.*, **177**, 1037–1049, doi:10.1111/j.1365-246X.2008.04084.x.
- Xie, J., Gok, R., Ni, J. & Aoki, Y., 2004. Lateral variations of crustal seismic attenuation along the INDEPTH profiles in Tibet from Lg Q inversion, *J. geophys. Res.*, **109**, B10308, doi:10.1029/2004JB002988.
- Yang, Y.J. & Forsyth, D.W., 2006. Regional tomographic inversion of the amplitude and phase of Rayleigh waves with 2-D sensitivity kernels, *Geophys. J. Int.*, **166**, 1148–1160.
- Yao, H., Xu, G., Zhu, L. & Xiao, X., 2005. Mantle structure from interstation Rayleigh wave dispersion and its tectonic implication in western China and neighboring regions, *Phys. Earth planet. Inter.*, **148**, 39–54.
- Yao, H., Van Der Hilst, R.D. & de Hoop, M.V., 2006. Surface-wave array tomography in SE Tibet from ambient seismic noise and two-station analysis—I. Phase velocity maps, *Geophys. J. Int.*, **166**, 732–744, doi:10.1111/j.1365-246X.2006.03028.x.
- Yao, H., Beghein, C. & Van Der Hilst, R.D., 2008. Surface wave array tomography in SE Tibet from ambient seismic noise and two-station analysis – II. Crustal and upper-mantle structure, *Geophys. J. Int.*, **173**, 205–219, doi:10.1111/j.1365-246X.2007.03696.x.
- Yin, A., 2000. Mode of Cenozoic east-west extension in Tibet suggesting a common origin of rifts in Asia during the Indo-Asian collision, *J. geophys. Res.*, **105**, 21745–21759.
- Yin, A., Kapp, P., Murphy, M., Manning, C.E., Harrison, T.M., Ding, L., Deng, X. & Wu, C., 1999. Significant late Neogene east-west extension in north Tibet, *Geology*, **27**, 787–790.
- Zeitler, P.K. *et al.*, 2001. Erosion, Himalayan geodynamics, and the geomorphology of metamorphism, *GSA Today*, **11**, 4–9.
- Zhao, W.L. & Morgan, W.J., 1987. Injection of Indian crust into Tibetan lower crust—a two-dimensional finite-element model study, *Tectonics*, **6**, 489–504.
- Zhao, W.J., Nelson, K.D. & INDEPTH Team, 1993. Deep seismic-reflection evidence for continental underthrusting beneath southern Tibet, *Nature*, **366**, 557–559.
- Zhao, W. *et al.*, 2001. Crustal structure of central Tibet as derived from project INDEPTH wide-angle seismic data, *Geophys. J. Int.*, **145**, 486–498.
- Zhao, W. *et al.*, 2007. Deep structure of the NE Tibetan Plateau: an introduction to Project INDEPTH, Phase IV, *EOS, Trans. Am. geophys. Un.*, **88**, Fall Meet. Suppl., Abstract T23G-06.
- Zhou, H.W. & Murphy, M.A., 2005. Tomographic evidence for wholesale underthrusting of India beneath the entire Tibetan plateau, *J. Asian Earth Sci.*, **25**, 445–457.
- Zhu, L. & Helmberger, D., 1996. Intermediate depth earthquakes beneath the India-Tibet collision zone, *Geophys. Res. Lett.*, **23**, 435–438, doi:10.1029/96GL00385.

SUPPORTING INFORMATION

Additional Supporting Information may be found in the online version of this article:

Supplement. The inversion for shear wave velocities is an underdetermined inversion problem. The dumping and smoothing strategy and the initial model should be determined carefully. We have tried different priori standard deviations of 0.05, 0.1, 0.15, 0.2, 0.25 and 0.3 km s⁻¹ for shear wave velocities to find the proper

dumping. The results are shown in Fig. S1. The difference of the mantle structure caused by different dumping parameters is insignificant compared with that of the crustal structure. We select a proper value of 0.1 km s^{-1} because the resultant model is smooth and deviates as much as possible from the initial model. We also conducted a random experiment to check the dependence on the initial model. We disturbed the shear wave velocities in all layers of initial model with random noises and ran the inversions with disturbed initial models 1000 times. The random noises are drawn from the uniform

distribution on the interval $(-0.1 \text{ km s}^{-1}, 0.1 \text{ km s}^{-1})$. The results are shown in Fig. S2. We find that the main features of the optimum model are unchanged despite disturbed initial models. Their effects on the optimum model are trivial.

Please note: Wiley-Blackwell are not responsible for the content or functionality of any supporting materials supplied by the authors. Any queries (other than missing material) should be directed to the corresponding author for the article.